Geophysical Journal International

Geophys. J. Int. (2026) **246,** 1–18
Advance Access publication 2026 May 13
Research Paper

https://doi.org/10.1093/gji/ggag182

Re-entry and burn up of Starlink-2382 satellite: estimating trajectory and ablation coefficient from acoustic and coupled seismic waves

D. Eickhoff,[1] J.-P. Föst[2,1] and J. R. R. Ritter[1]

[1]*Karlsruhe Institute of Technology, Geophysical Institute, 76187 Karlsruhe, Germany. E-mail: dario.eickhoff@kit.edu*
[2]*RWTH Aachen University, Teaching and Research Area Neotectonics and Natural Hazards, 52064 Aachen, Germany*

Accepted 2026 May 4. Received 2026 April 24; in original form 2025 September 29

SUMMARY

On 2024 August 27th, at approximately 19:30 UTC, the Starlink-2382 satellite entered the Earth's atmosphere following an uncontrolled re-entry manoeuvre over Central Europe. This event resulted in a relatively low-angle re-entry of the satellite into the atmosphere, which might have provided sufficient time to burn up the satellite before reaching the Earth's surface. This study employs acoustic-seismic (A-S) data from 226 recording stations to analyse the trajectory of Starlink-2382′s re-entry, utilizing 3-D atmosphere models including wind data and acoustic ray tracing methods. To identify signals emitted by the falling satellite, we process A-S recordings of Austrian, French, German, Italian, Slovenian and Swiss regional seismic networks. We compute the satellite trajectory with a novel ray-based direct-search optimization method and find an azimuth angle of $120.5^\circ \pm 0.4^\circ$ from North and an initial elevation angle of $1.5^\circ \pm 0.7^\circ$, together with an entry velocity of approximately 8.9 ± 0.7 km s^{-1}. Our findings indicate that this acoustic-seismic approach, including traveltime effects due to wind, achieves a better fit to our large data set compared to the trajectory solutions from optical methods in this specific context. Furthermore, we calculate an effective ablation coefficient of 0.11 ± 0.02 s^2 km^{-2} for the main satellite fragment. Within the limits of this estimate, this is consistent with a scenario in which the main fragment, with a mass of c. 100 kg could have experienced near-complete ablation during atmospheric descent.

Finite-difference modelling illustrates the complex acoustic wavefield resulting from the satellite's deceleration and shows the expected widening of the Mach Cone. This highlights the importance of accounting for trajectory curvature and time-varying Mach angles when modelling acoustic wave propagation from low-angle re-entering objects. For recording sites with both, acoustic (infrasound) and seismic sensors, the acoustic-to-seismic ground coupling coefficients are determined. These vary up to three orders of magnitude, from 4.31×10^{-10} to 5.86×10^{-7} m s^{-1} Pa^{-1} across our station sites, which is primarily explained by differences in stiffness of surface rocks.

Key words: acoustic emission; acoustic-gravity waves; infrasound; numerical modelling; seismic instruments; wave propagation.

1. INTRODUCTION

The presence of uncontrolled satellites in Low-Earth Orbits (LEOs) poses considerable economic as well as social risks. This threat manifests in the form of potential hazards to existing satellites, manned space missions, infrastructure and even lives on Earth's surface (R.P. Patera 2008; W.H. Ailor 2019; P. Omaly *et al.* 2025). Related risks increase with the rapidly accumulating number of objects occupying LEOs (A. Lawrence *et al.* 2022). The recent development of megaconstellation communication-satellite networks, which provide commercial satellite-based internet access, resulted in a significant increase in the number of LEO objects (McDowell, 2020). A leading driver to provide satellite-based internet access is the U.S. company SpaceX with about 7000 satellites for the Starlink service (SpaceX 2025). On August 27th at approximately 19:30 UTC, the Starlink-2382 satellite re-entered Earth's atmosphere above France (see Fig. 1b). This event occurred after SpaceX lost control over the satellite that led to an uncontrolled re-entry of the spacecraft over Central Europe in contrast to the target region of open oceans, away from populated islands and heavily trafficked airline and maritime routes (SpaceX 2025). SpaceX asserts that a Starlink satellite should completely burn up during an atmospheric re-entry (SpaceX 2025). Here we want to use this uncontrolled satellite re-entry to investigate the likelihood of a full burn-up during re-entry and compare the satellite's rate of ablation with other re-entry events. Our study benefits from a high number of recording stations in Central Europe and a low-elevation angle which causes a strong wave emission towards the Earth's surface. The partly known parameters of the satellite

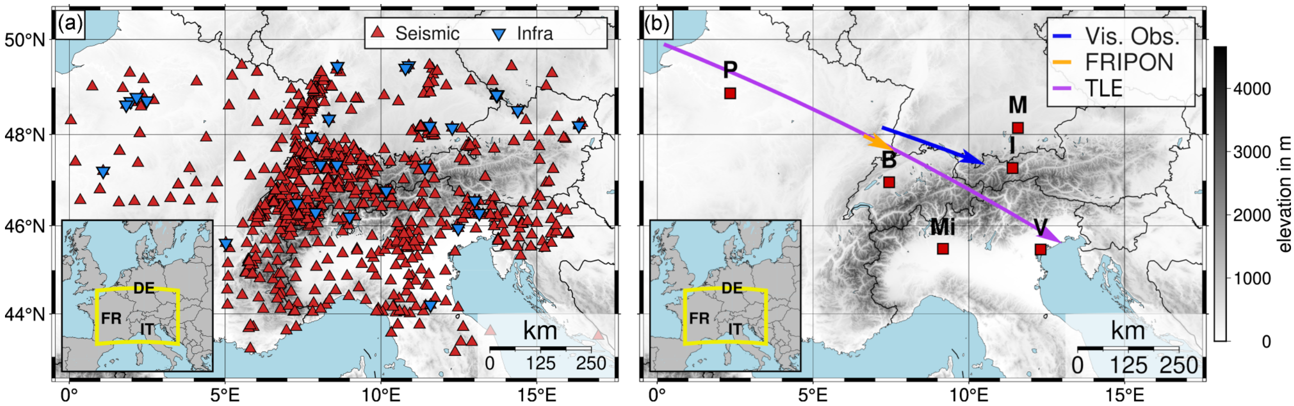

Figure 1. (a) Map of the target region in Central Europe. Red triangles indicate seismic stations, while blue inverted triangles denote infrasound stations from which data were retrieved. The inset map illustrates the geographical location of the target region within Europe. (b) Three trajectories are given, derived from human observations in blue (IMO 2024), the meteor observation camera network FRIPON (2024) in yellow, and satellite TLE data in purple (E.A. Satcat 2024). The inset map indicates the position within Europe. Larger cities for orientation are Paris (P), Bern (B), Milano (Mi), Innsbruck (I), Munich (M) and Venice (V).

for example, mass, offer an advantage compared to meteoroid observations. Such *a priori* information helps to test methods which are also applied to study meteoroid properties such as mass or kinetic energy.

When an object enters Earth's atmosphere with a velocity v exceeding the local speed of sound (v_s), acoustic Mach waves are generated. For $v >> v_s$, the wavefronts of these Mach waves travel almost parallel to the fast-moving object producing the waves (e.g. W.N. Edwards, D.W. Eaton & P.G. Brown 2008). The following interaction and deformation of the Earth's crust, induced by these acoustic waves and recorded with seismometers, can be used to invert for trajectory parameters of the flying object (e.g. H. Kanamori *et al.* 1992; S.J. Arrowsmith *et al.* 2007; W.N. Edwards *et al.* 2008; B. Fernando & C. Charalambous 2026).

In the region of Central Europe, beneath the re-entry trajectory of Starlink-2382 satellite, there are some of the world's most extensive seismic station networks (Fig. 1a), a circumstance that facilitates a comprehensive study of the re-entry. The geology underneath the recording stations can be broadly categorized into poorly consolidated sediments in the northern and southern foreland basins of the European Alps and hard rock in the mountainous Alpine region (O.A. Pfiffner 2021). This petrophysical difference may cause varying coupling coefficients for the conversion of acoustic to seismic waves (e.g. W.N. Edwards, P.G. Brown & D.W. Eaton 2009; A. Novoselov, F. Fuchs & G. Bokelmann 2020; B. Fernando *et al.* 2024a).

Previous investigations (H. Kanamori *et al.* 1992; A. Qamar 1995; J.E. Cates & B. Sturtevant 2002; C.A. Langston 2004; J. Pujol, P. Rydelek & T. Bohlen 2005; C.D. De Groot-Hedlin *et al.* 2008; W.N. Edwards *et al.* 2008) have demonstrated that the use of seismic recordings can serve to constrain meteoroid as well as spacecraft trajectories. In a similar manner, acoustic recording data from infrasound stations can be utilized (e.g. W.N. Edwards 2009; C.D. de Groot-Hedlin & M.A. Hedlin 2014; C. Pilger *et al.* 2020). One objective of this study is to compare the accuracy of different acoustic-seismic (A-S) trajectory solutions, such as geometrical and ray-based methods together with finite-difference wavefield modelling, with the results provided by human observations, camera recordings and the two-line element set (TLE) data of the satellite.

The acoustic waveform data can be also used to extract the (kinetic) energy of the moving object. In this study, another objective is to investigate the energy of the moving source and the rate at which acoustic waves induce seismic waves into the subsurface. This is achieved by analysing colocated A-S recording stations. First, the change of the source energy along the satellite's fall trajectory will be analysed and then the A-S coupling efficiency. Additionally, the change of energy of the source will be related to a change of satellite mass due to the ablation processes. Understanding the local A-S coupling coefficients is important to constrain future space-debris or meteoroid masses based on ground motion measurements and relationships between acoustic wave amplitudes and source energies (D.O. ReVelle 1997).

1.1 Acoustic and seismic data

The A-S data for this study is obtained through the International Federation of Digital Seismograph Networks (FDSN, see Network References), and the study area encompasses a total of 1376 seismic recording stations and 34 infrasound recording stations from 36 networks. Ten infrasound stations are colocated with seismic sensors. We use the TLE data of the satellite to further constrain the search area. We restrict the analysis to stations where the expected acoustic wave arrival is within 1000s after 19:28:00 UTC. This reduces the data set of 1410 individual stations to 611 seismic and 12 acoustic stations. The vertical recording component of the seismic data was analysed to determine the first onset of the A-S coupled wave. A deconvolution was applied to transform the waveform amplitudes to true ground motion velocity. Afterwards a non-zero phase high-pass filter with a cut-off frequency of 1 Hz was applied to the seismic waveforms. The infrasound recording data was processed in a similar manner and the waveform amplitudes were transformed to

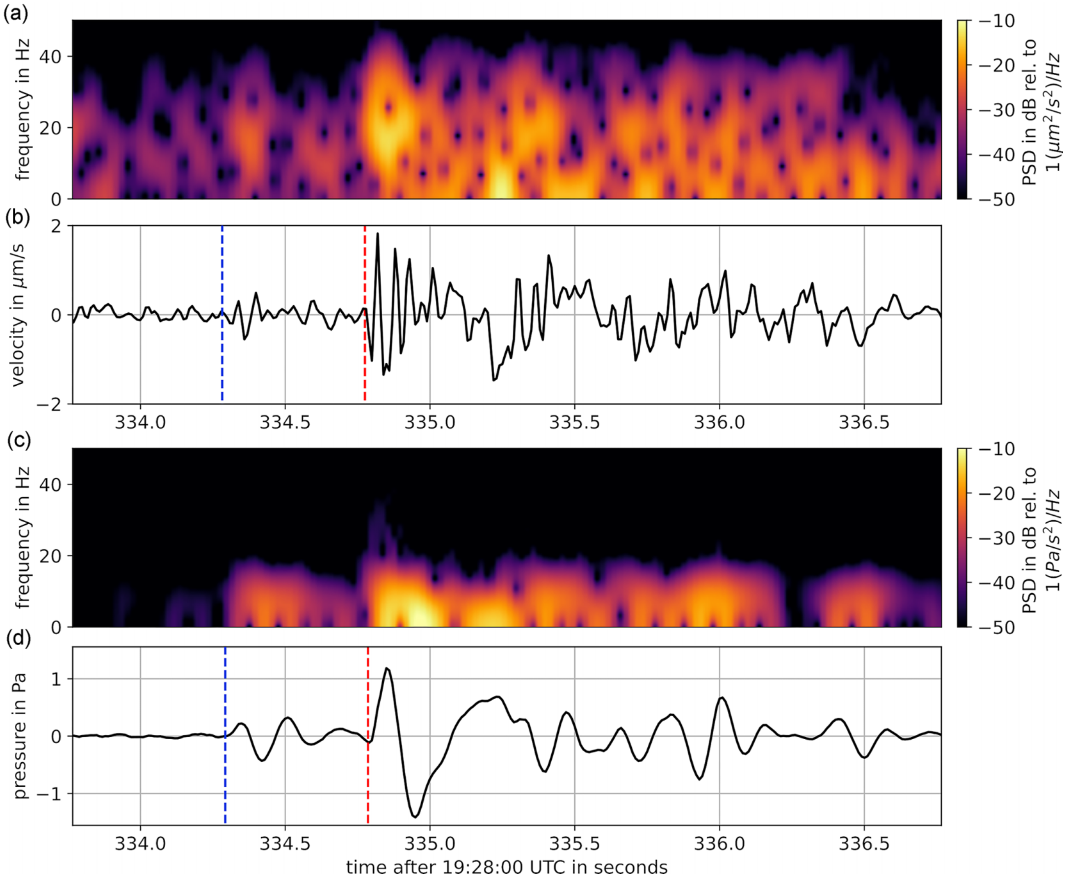

Figure 2. Observed recordings at Raspberry Shake & Boom station AM.R03EA, located within 10 km distance of the centre line (see Fig. 3). (a) Spectrogram of the vertical component of the seismic recording. Colours are scaled to the maximum measured spectral amplitudes. (b) Waveform of the seismic recording data in μm/s. The red dashed line marks the onset of measured W-shaped wavelet associated with the A-S coupled wave. The blue dashed line marks the onset of a wave due to a possible smaller fragment of the satellite which is ca. 0. 5 s ahead, an air-coupled Rayleigh wave (e.g. W.N. Edwards *et al.* 2008) or a faster multipathing event. (c) Spectrogram of the infrasonic recording. Colours are scaled to the maximum measured spectral amplitudes. (d) Waveform of the infrasound recording data in Pa. The red dashed line marks the onset of a measured N-shaped wavelet associated with the acoustic wave.

pressure. Due to the significantly lower frequency nature of the acoustic waves, the data was high-pass filtered with non-zero phase and a corner frequency of 0. 1 Hz (see Fig. 2). The lower frequencies of the infrasonic acoustic waves also result in detection ranges over thousands of kilometres (D.O. ReVelle 1976; C.D. de Groot-Hedlin & M.A. Hedlin 2014).

Out of the 611 seismic recording stations, the A-S coupled wave signals could be identified at 218 of these stations. This results in a recovery rate of approximately 36 per cent. For shielding reasons, seismological recording stations are often placed in locations where short-period pressure differences, such as acoustic waves, should not disturb the instruments. This is a critical aspect of earthquake seismology, but it hinders the detection of acoustic non-earthquake events, such as this satellite fall. Notably, the density of seismic recording stations in this area is exceptionally high, particularly given that it is an unplanned re-entry, as opposed to the planned recording efforts for missions such as OSIRIS-REx (e.g. B. Fernando *et al.* 2024a, b; E.A. Silber *et al.* 2024), Hayabusa (e.g. M.Y. Yamamoto *et al.* 2011; Y. Ishihara *et al.* 2012) and Hayabusa2 (e.g. Y. Nishikawa *et al.* 2022; E.K. Sansom *et al.* 2022). In terms of infrasound recording stations, these demonstrate clearly enhanced detection efficiency as no A-S coupling is involved: of the 12 infrasound stations, eight were able to detect clear acoustic wave signals, resulting in a recovery rate of approximately 66 per cent.

In summary, we identify signals related to the satellite re-entry at 218 seismic and 8 infrasound stations, yielding 226 total arrival times as data distributed across Austria, France, Germany, Italy, Slovenia and Switzerland. From the isolines of the signal-arrival times (see Fig. 3a), we derive an initial approach trajectory based on A-S data alone. This trajectory fits quite well with the projected trajectory of the TLE data of the satellite (E.A. Satcat 2024). A significant non-random systematic offset is observed when comparing the average apparent acoustic wave velocity for stations located north and south of the initial trajectory (Figs 3b and c). This offset suggests that the signals arrive faster at stations north of the trajectory, hence with a higher apparent average velocity along their respective wave travel paths compared to stations south of the trajectory (see Figs 3b and c). This offset could be related to a SW–NE wind below ca. 50 km height (Fig. 4) with an upwind effect towards SW slowing down acoustic waves and a downwind effect towards NE with acoustic waves becoming faster.

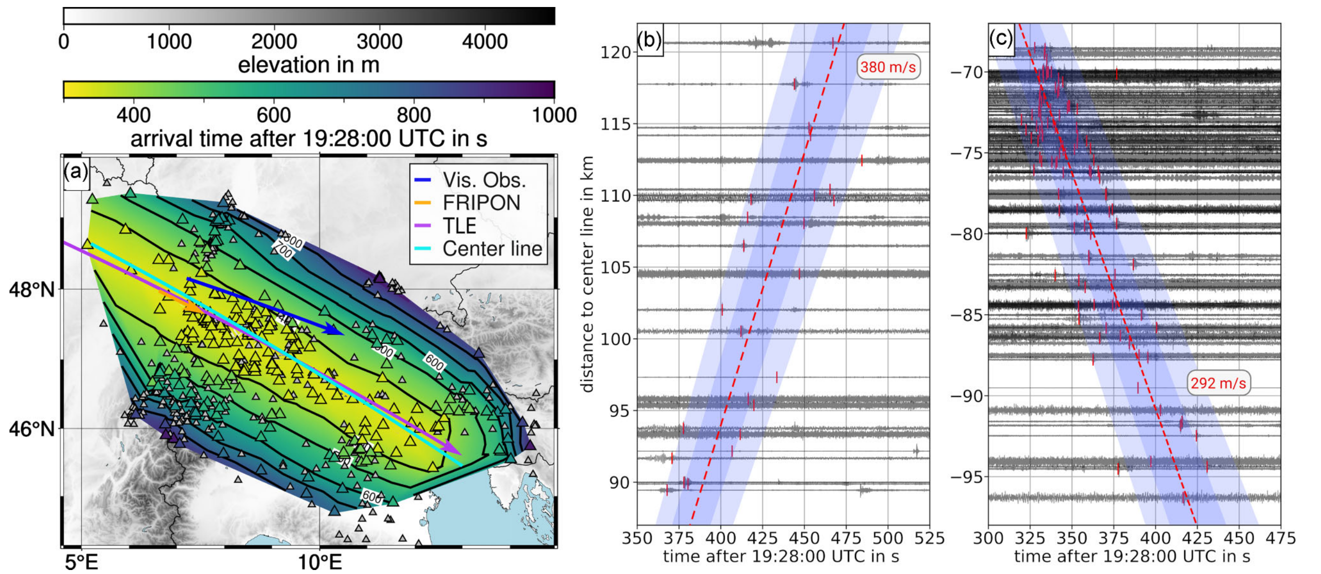

Figure 3. (a) Map of the target region displaying the locations of acoustic and seismic recording stations (triangles). The triangles are colour-coded according to the arrival time of the acoustic or seismic wave, respectively. Grey triangles are stations where no signal could be identified. Contour lines represent interpolated arrival times, and the colour gradient gives a smooth picture of the spreading wave. Trajectories of the IMO (2024) (blue), FRIPON (2024) (yellow) and Starlink-2382 satellite TLE data (purple; Satcat 2024) are also displayed. Additionally, a centre line (cyan) is derived geometrically from the minimum of the arrival time contours. (b) Record section with acoustic and seismic waveforms located to the north of the centre line. The first onset times of the acoustic wave signals are marked with a red vertical bar, and the average apparent propagation velocity is marked with a red dashed line. Dark blue areas indicate deviations of the average velocity of up to 5 per cent, while light blue areas indicate deviations of up to 10 per cent. (c) The same as panel (b), but for waveforms located to the south of the centre line.

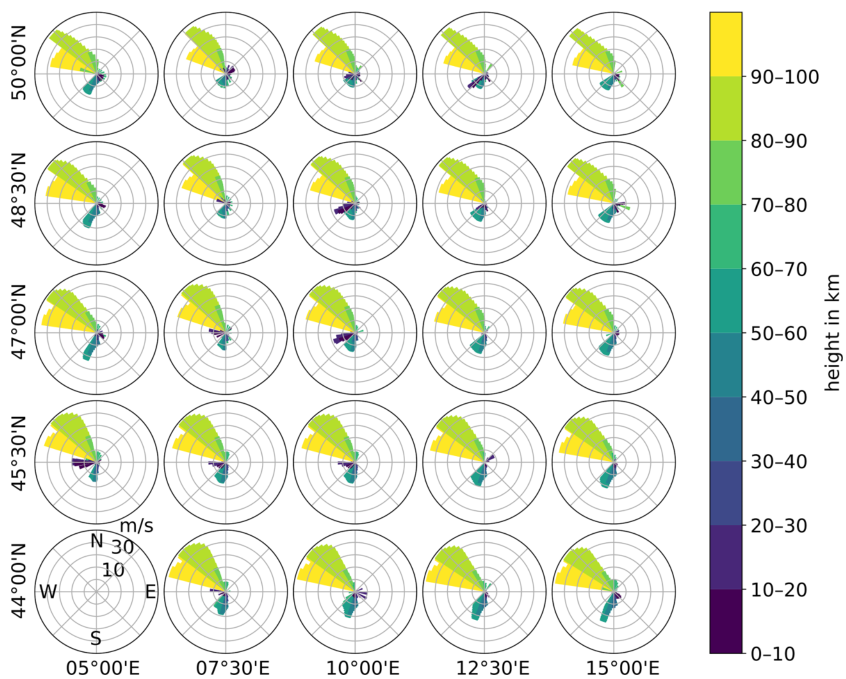

Figure 4. Grid of polar plots with 1.5° distance in N–S direction and 2.5° distance in W–E directions displaying wind direction, speed and height (colour). The direction of the colour-coded bins corresponds to the wind direction. The length of the bars denotes wind speed, ranging from 0 to 50 m s^{-1} (one circle corresponds to a 10 m s^{-1} increment). Each position of a polar plot within this grid corresponds to the location of its respective 1-D atmospheric model, which was employed to calculate these wind directions and speeds. Data is provided by the NCPAG2S-Client (NCPAG2S-CLC: Hetzer, C.H., 2024) .

In order to better understand the origin of this offset, it is necessary to incorporate more complex atmospheric models for acoustic velocity that include a stratified atmosphere and wind for the trajectory-reconstruction approach. To this end, a 3-D grid compiled from 1-D ground-to-space atmosphere models is utilized (D.P. Drob, J.M. Picone & M. Garcés 2003; D.P. Drob *et al.* 2010). The highest wind speeds occur in the thermosphere and mesosphere (above 50 km altitude), with speeds of up to 50 m s^{-1} and a uniform north-westerly direction at all grid points (Fig. 4). In the stratosphere (20–50 km altitude), the wind direction shifts to south–southwest, with average speeds of 10 m s^{-1}. Below altitudes of 20 km, the wind direction appears to be more random, which is expected for the troposphere as it is dominated by smaller-scale weather phenomena (e.g. M. Huber *et al.* 2001; L. Mahrt 2011).

2. METHODS

To determine the optimal trajectory solution, the particle swarm optimization (PSO) method proposed by D. Vida (2023) is applied, which is an improved application of the inversion derived by J. Pujol *et al.* (2005). We call this method, that derives trajectories from geometrical rays, the geometrical model in the following. This method is implemented to identify a linear trajectory that minimizes the arrival time residual over all acoustic and seismic traveltime readings. The trajectory is constrained by six parameters: The puncture point P of the trajectory with the Earth's surface as P(x_0, y_0, t_0), as well as the elevation angle θ, the azimuth angle φ and the velocity v. The analysis minimizes the cost function L to find the optimal trajectory solution:

$$L=\sum_{i=1}^{N} 2\left(\sqrt{1+(t_{\mathrm{a,i}}-t_{\mathrm{o,i}})^2}-1\right). \tag{1}$$

Here the analytical arrival time $t_{\mathrm{a,i}}$ is defined as the time when the acoustic or seismic signal arrives at the observation point i, as described by J. Pujol *et al.* (2005) and D. Vida (2023) for a Mach Cone in the atmosphere. The observed arrival time $t_{\mathrm{o,i}}$ is defined as the onset time of the identified acoustic or seismic wave arrival at the observation station i. To determine the optimal trajectory that explains our arrival time measurements, we applied the PSO as implemented in the PySwarms (PySwarms: Miranda, 2018) Python library. However, it should be noted that this implementation of the geometrical method is subject to certain limitations and assumptions: (1) a constant sound velocity in the atmosphere which was fixed at 320 m s^{-1}, (2) linear travel paths from the trajectory to the A-S stations and (3) a straight trajectory with a constant velocity (e.g. J. Pujol *et al.* 2005; D. Eickhoff *et al.* 2023; J.-P. Föst *et al.* 2023; D. Eickhoff, J.P. Föst & J. Ritter 2024; Föst, Eickhoff & Ritter, in preparation). The geometrical model is applied as a two-step process: In the first step, the cost function is minimized with all 226 arrival time observations. In the next step, arrival times with a residual greater than 20 s are eliminated, and then the geometrical model is reiterated. The initial parameters for both geometrical model runs of a given iteration are both defined by the same geometrical trajectory (see Fig. 3a). For our application, we use 216 arrival times and invert for six parameters, which is a well-posed inversion problem.

To find the optimal trajectory, 500 two-step geometrical model runs are performed, generating 500 trajectories. The goodness of their fit is measured by their arrival time residual. These are displayed as blue bars in Figs 5a, c and d within the target region. The best-fit geometrical model trajectory has azimuth and elevation angles of approximately 120° and 12°, respectively, and an average satellite velocity of approximately 8 km s^{-1}. The root mean square error (short: RMSE) of our geometrical model is approximately 10. 9 s based on 161 arrival times.

In most of the geometrical model runs, stations close to the geometrical centre line are not excluded after the first step. This is expected, as only for more distant stations the assumption of linear rays leads to large arrival time residuals that the method cannot balance anymore. This is further illustrated by stations located at the periphery of the modelling region, which are identified as potential candidates for removal following the initial PSO step, because their residual often exceeds 20 s (see Fig. 5b). This outcome is attributed to the violation of assumptions (1) constant velocity and (2) straight ray paths. For stations distant from the trajectory, the average velocity of a pressure wave arriving at the station is likely to deviate from the anticipated 320 m s^{-1}, as atmospheric conditions such as wind significantly influence the propagation speed. As demonstrated in Fig. 4, the wind velocity in the target region is in the order of magnitude of tens of m s^{-1}. For long travel paths, the impact of wind disturbances on the average velocity becomes more pronounced. Assumption (2) is violated due to the impact of winds on the propagation of the pressure wave, resulting in a curvilinear travel path. Furthermore, Fig. 5(e) reveals systematic deviations in the arrival time residuals. Negative residuals are observed to the north of the trajectory, indicating that the acoustic wave velocity exceeds the average speed of sound of 320 m s^{-1}. Conversely, the stations positioned south of the trajectory predominantly exhibit positive arrival time residuals, indicating that the acoustic wave propagates at a velocity that is less than 320 m s^{-1}. The gridded wind model (Fig. 3) suggests that this spatial distribution of arrival time residuals can be attributed to the preferential winds with a predominant north–northwest orientation within the lower 50 km in the atmospheric layers.

Consequently, an improved approach to reconstruct the satellite trajectory was developed that includes the wind parameters. This approach is based on infraGA/GeoAc (P. Blom 2014) to enhance the solution of the geometrical model. The programme infraGA encompasses a ray tracer that allows the use of complex atmospheric weather models as input. We use a native functionality of infraGA that enables the simulation of supersonic trajectories and their associated arrivals from an approximated Mach wave at the Earth's surface (P. Blom *et al.* 2024). We apply an iterative damped direct search to identify new trajectory candidates that are then evaluated with the infraGA to achieve a so-called ray model. We use the best-fitting geometrical model trajectory solution as the initial guess

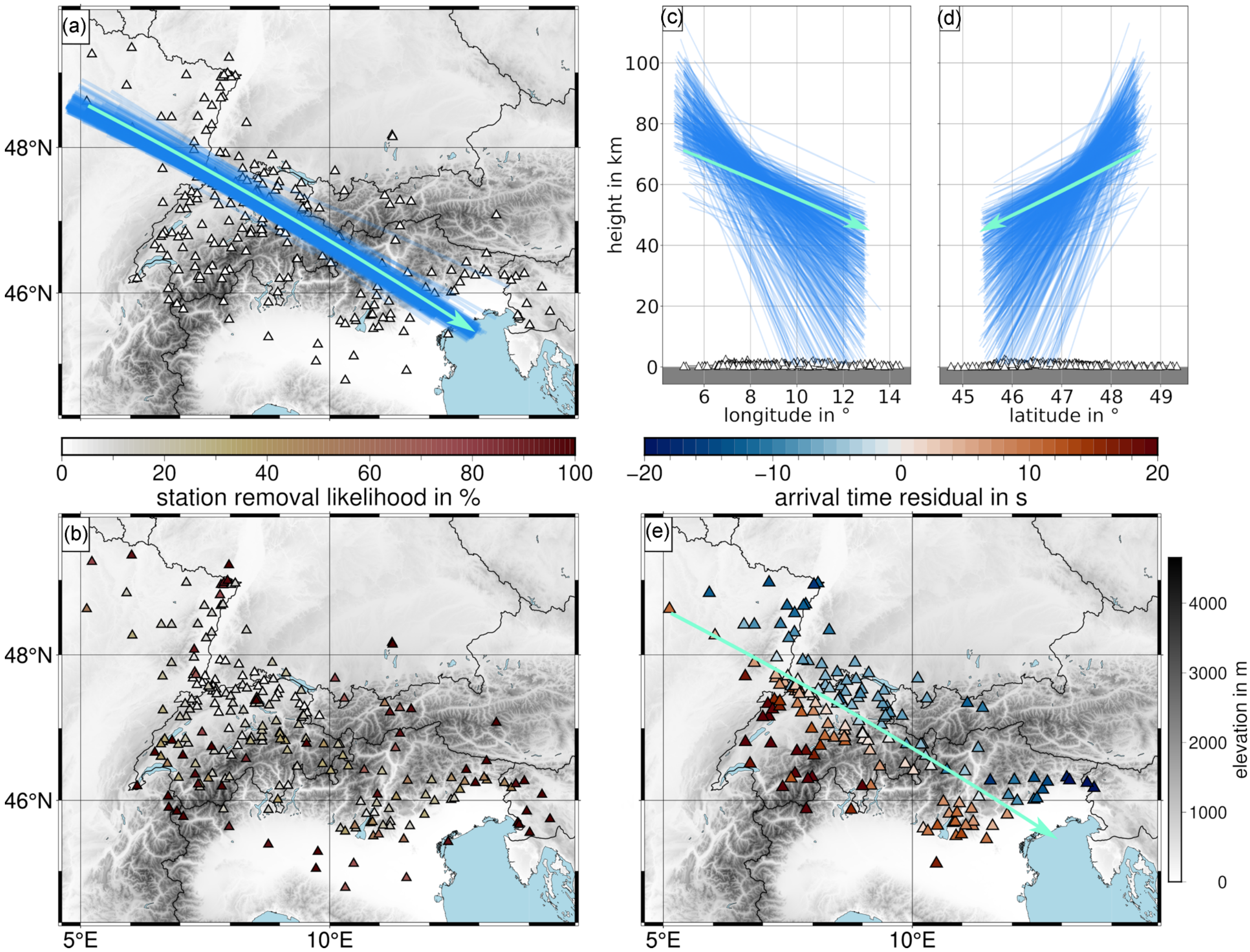

Figure 5. (a) Map showing different trial trajectories of the geometrical model reconstruction method in transparent blue. The optimal geometrical model trajectory is highlighted in cyan, while white triangles indicate seismic and acoustic recording stations. The colour-coding of trajectories and symbols is consistent with panels (c)–(e). (b) Map of A-S stations and their likelihood of removal during the calculation of the geometrical model solution. Panels (c) and (d) illustrate the E–W versus height and N–S versus height distribution of the trial trajectories, respectively. Panels (c) and (d) are shown with a c. 6 times exaggerated height scale. Panel (e) shows a map of the arrival time residuals, with blues representing negative and reds representing positive traveltime residuals for the optimal geometrical model trajectory.

to calculate rays that minimize the wind effects on our trajectory solution using the gridded 3-D wind model shown in Fig. 4. This approach allows us to use: (1) a realistic atmospheric model, (2) curved ray paths that adhere to the physics of atmosphere and can be bent by wind and velocity changes and (3) trajectory geometries that allow for deceleration and bending of the trajectory due to wind and gravity. By taking advantage of these features, we are able to overcome the restrictive assumptions of the geometrical model and model a more realistic re-entry trajectory of Starlink-2382 satellite and its associated A-S signals. One of the drawbacks, however, is that including the topography and thus the elevation of the A-S stations leads to an increase in computing time of roughly ten times. Because of that, we manually correct the wave arrival times for elevation, by adding the traveltime of an inclined acoustic wave between the station elevation and sea level, similar to station corrections used in seismological applications (E. Kissling, W.L. Ellsworth & D. Kradolfer 1994). To do this we use the PSO solution and calculate the Mach Cone for that trajectory. With the inclination angle of the nearest ray arrival to each station, we correct their elevation with the assumption that trajectory geometry will not change significantly between different trajectory evaluations.

To better understand the wavefield generated by the downward bending trajectory of the Starlink satellite and the progressive opening of the Mach Cone as the satellite decelerates, we extended our analysis with a finite-difference (FD) wavefield modelling (short: FDM). This approach follows the methodology described by Föst *et al.* (in preparation) for meteoroid-induced acoustic and seismic signals.

The wavefield of the last segment of the trajectory (c. 360 km) was modelled using the WAVE-Toolbox (T. Qin & T. Bohlen 2022), applying a 3-D FD scheme to solve the elastic wave equation on a high-performance computing grid. The moving supersonic source was implemented as a sequence of time-shifted point sources along the pre-computed trajectory, capturing the generation and evolution of the Mach Cone and its interaction with the Earth's surface. The time-shift is calculated accordingly from the velocity and flight path of the object along the trajectory. For the point source function, we used a Fuchs–Müller wavelet (K. Fuchs & G. Müller 1971), with a centre frequency of 0. 05 Hz. The low frequency makes it possible to set the grid distance to 250 m avoiding grid dispersion effects. However, in this way we just model the lowest frequencies from the shock wave, which is sufficient enough to investigate the wave propagation and the first arrival behaviours. For the interpretation of the modelled signals this frequency limit should be accounted for.

As velocity model, we used the atmospheric model described in Section 1, excluding wind effects. To model the coupling into seismic waves, a solid Earth layer was included in the velocity model with a *P*-wave velocity of 4700 m s^{-1} and an *S*-wave velocity of 3000 m s^{-1}. Modelling parameters were selected based on grid stability conditions to ensure minimal numerical dispersion, following Föst et al. (in preparation). The used parameters and modelling details are provided in the Supplementary Material.

3. TRAJECTORY AND ABLATION MODELLING

To calculate the trajectory of the satellite we begin with calculating its speed. For that we follow the methodology of M.D. Campbell-Brown *et al*. (2013) and Z. Ceplecha *et al*. (1998), where the speed is calculated based on the conservation of momentum

$$\frac{\mathrm{d}v}{\mathrm{d}t} = \frac{\Gamma \rho_a v^2}{m} A \left(\frac{m}{\rho_\mathrm{m}}\right)^{\frac{2}{3}}, \quad (2)$$

with the shape factor A, the drag coefficient Γ and the time-dependent mass m of the satellite

$$A = S\left(\frac{\rho_\mathrm{m}}{m}\right)^{\frac{2}{3}}, \quad (3)$$

where ρ_a is the atmospheric density, v is the speed of the satellite, ρ_m is the density of the satellite and S is the cross-sectional area of the satellite. For simplicity we assume that the satellite spins randomly while re-entering and that we can assume a spherical body, which is mostly made of aluminium (A.C. Boley & M. Byers 2021) with a density of c. 2700 kg m^{-3}. As shown by R.T. Carter, P.S. Jandir & M.E. Kress (2011) the drag coefficient is Mach number dependent, and we use their derived functions to calculate the drag coefficient Γ dynamically

$$\Gamma(M) = 0.5 \begin{cases} 0.45M^2 + 0.424, & 0 \le M \le 1.15 \\ 2.1\exp(-1.2(M+0.35)) - 8.9 \quad \exp(-2.2(M+0.35)) + 0.92, & M > 1.15 \end{cases} \quad (4)$$

where M is the Mach number. To account for ablation in our modelling we use the classical approach, by which mass loss can be described by ablation and fragmentation. For this we follow M.D. Campbell-Brown *et al*. (2013) and define mass loss as

$$\frac{\mathrm{d}m}{\mathrm{d}t} = -\Gamma \mathrm{A} \left(\sigma + \sigma_e\right) \left(\frac{m}{\rho_\mathrm{m}}\right)^{\frac{2}{3}} \rho_a v^3, \quad (5)$$

where the ablation coefficient is σ. The starting parameter for the ablation of $\sigma = 0.1$ s^2 km^{-2} is chosen to reflect a complete mass loss, where the end particle mass is <1 per cent of the original mass. The satellite separated into multiple individual fragments during re-entry (see Fig. S1 and Table S2 in Supplementary Material), but because there is little detailed information available on this and especially the detached masses are unknown, we opt to model the Mach wave of the main satellite fragment. The original wet mass of the satellite is 260 kg. Because the satellite was roughly halfway into its lifecycle and the dry mass is 248 kg, we assume that the satellite has a mass of at least 254 kg. We also assume that about 95 per cent of the original mass should be accounted for along the portion of our trajectory. As the atmospheric density increases exponentially (and thus ablation increases) with decreasing altitude, we extrapolate the geometrical model solution parameters to a higher altitude of 85 km to use it as starting altitude for the ray model.

At this altitude the mass loss from ablation begins to significantly affect the satellite (M.D. Campbell-Brown *et al*. 2013). We subtract an additional estimated 10 per cent, or about 25 kg of the satellite mass to account for those parts of the satellite which will break off in the beginning during re-entry, namely the solar panels. This estimation leads to an approximate initial mass of 220 kg of the main body before the start of our modelled trajectory. Additionally, we analyse available photos and videos of the re-entry to estimate fragmentation. In Fig. S1 (Supplementary Material), the observational points and in Table S2 (Supplementary Material), the identified fragments are listed. We find that the satellite separated into multiple fragments during its atmospheric flight path and identified one main fragment which seems to encompass about half of the original size. Thus, we assume a mass of c. 100 kg for the main fragment, to estimate the mass loss due to ablation. Because of this, we set $\sigma_e = 0$ to disallow further disintegration of the main fragment. Furthermore, the satellite's distinct fragmented masses may have caused the precursor signal identified in Fig. 2. Using eqs (2)–(5), we determine gravity-, wind- and ablation-affected trajectories of this main fragment and use it as input for the ray model. In contrast to the gravity and wind effects the ablation of the main fragment is additionally inverted for in the ray model.

To fully define the modelled trajectory of a given iteration we define a starting point of the trajectory as well as an initial azimuth, elevation angle and initial velocity (see Table 1). The solution of the geometrical model results in an averaged velocity for the main fragment of the satellite along the trajectory. For the ray modelling we use the starting velocity of 8 km s^{-1}, which is also in agreement

Table 1. Comparison of trajectory parameters start longitude, start latitude, start altitude, start velocity, azimuth angle φ, elevation angle θ and ablation coefficient σ for the different methods. IMO (2024), FRIPON (2024), TLE (E.A. Satcat 2024), our Geometrical and Ray models.

	IMO	FRIPON	TLE	Geometrical model	Ray model
Lon_{start} in °E	4.69 [a]	4.69 [a]	4.69[a]	4.8	4.69 ± 0.08
Lat_{start} in °N	48.76[a]	48.63[a]	48.4[a]	48.6	48.76 ± 0.06
alt_{start} in km	80	74.8[b]	n/a	75.6	74.0 ± 3.2
v_{start} in km s^{-1}	n/a	c. 10	c. 7.8 [c]	8	8.9 ± 0.6
φ in °	108.5	116	113	120	120.5 ± 0.4
θ in °[d]	19.5	n/a	n/a	12	1.1 ± 0.7
σ in $\mathrm{s}^2\,\mathrm{km}^{-2}$	n/a	n/a	n/a	n/a	0.11 ± 0.02
β in s^{-1}	n/a	n/a	n/a	n/a	0.02 ± 0.005

[a]Lat/Lon values were matched to the start locations of best-fit trajectory.
[b]At the start of trajectory (Fig. 1b, 5b).
[c]From TLE data.
[d]For IMO and the geometrical model the elevation angle is constant along the trajectory.

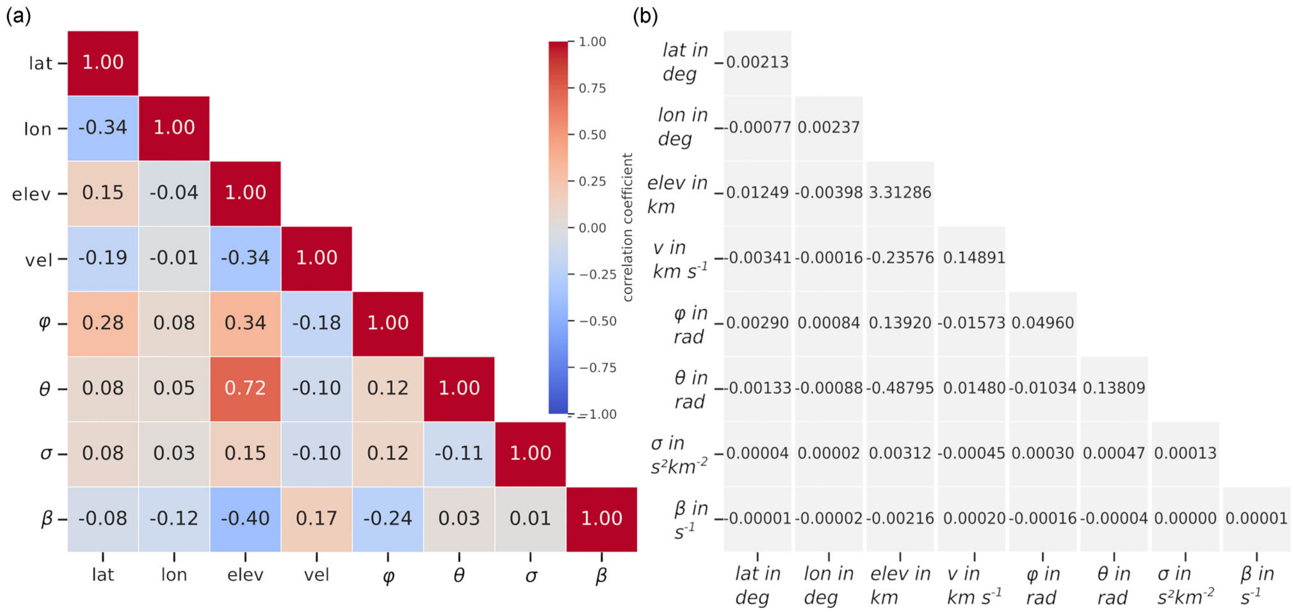

Figure 6. (a) Correlation matrix for the eight inverted parameters of the satellite trajectory (lat: latitude; lon: longitude; elev: elevation; vel: velocity; φ : azimuth angle; θ : elevation angle; σ: ablation parameter; β: lift parameter). (b) Covariance matrix for the eight inverted parameters of the satellite trajectory. Units at the axes are the ones used for calculating the covariances. Note that due to the different units and scales of each parameter, the resulting off-diagonal covariances are difficult to interpret.

with the velocity calculated from the TLE (see Table 1). In the ray modelling we fix the start time to 85 s after the reference time of 19:28 UTC using the event time gathered from the camera network (FRIPON 2024) to reduce the number of free parameters by one.

The inversion for the trajectory calculation contains not only the ablation σ, but also an additional parameter β which corrects the vertical velocity change due to a lift-like force, that is, the Magnus effect, which is related to the possible uncontrolled spinning of the satellite (e.g. J. Elliott *et al.* 2024; S. Mancuso, D. Barghini & D. Gardiol 2024). This modifies eq. (2) and we obtain the following expression for our improved ray modelling:

$$\frac{\mathrm{d}v_z}{\mathrm{d}t} = -g - \frac{\Gamma \rho_\mathrm{a} v v_z}{m} A \left(\frac{m}{\rho_\mathrm{m}}\right)^{\frac{2}{3}} - \beta v_z, \ \mathit{with}\ v = \sqrt{v_x^2 + v_y^2 + v_z^2}. \tag{6}$$

4. RESULTS

4.1 Trajectory

Using the ray model, including the effects of wind and a stratified atmosphere, we find the optimal trajectory solution with eq. (6) and the eight parameters defined as in Table 1. This solution has a minimum arrival time residual value after evaluating approximately 4500 trial trajectories. The arrival time residuals of the best-fit ray model trajectory (Fig. 7b) do not have the systematic north–south

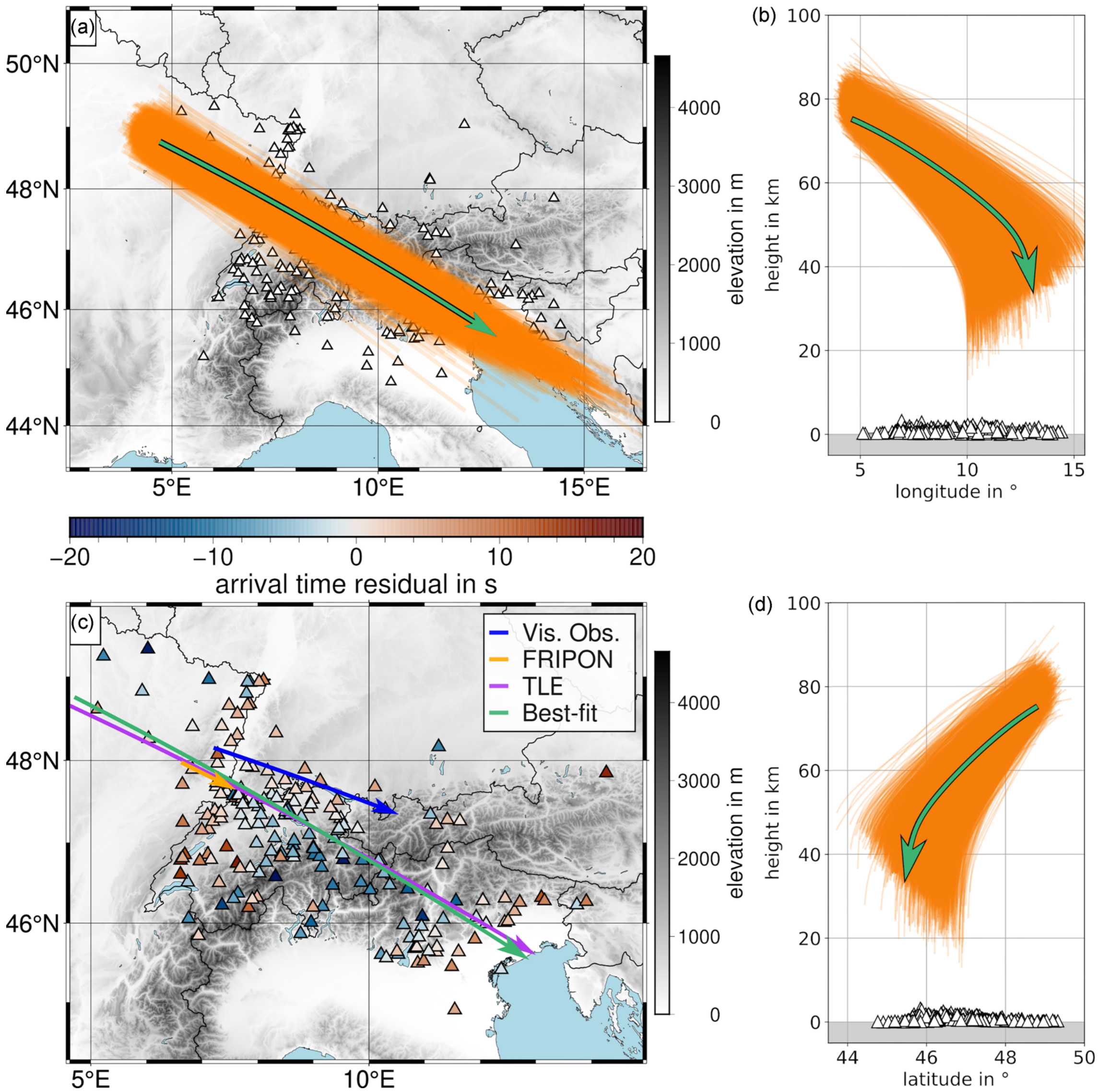

Figure 7. (a) Map showing different trial trajectories of the ray model reconstruction method in transparent orange. In green the best-fit ray model trajectory is shown. White triangles mark seismic and acoustic stations. This colour-coding of trajectories and symbology is the same in panels (b) and (d) as well. Panels (b) and (d) show the E–W and N–S versus height distribution of trajectories, respectively (with a c. 6 times exaggerated height scale). (c) map of the arrival time residuals. Blues represent negative and reds represent positive arrival time residuals for the best ray model trajectory.

deviations with respect to the geometrical model trajectory (Fig. 5d). Instead, they seem to have a NW–SE (positive to negative to positive residuals) trend along the trajectory.

The solution can be evaluated with a correlation analysis (see Fig. 6a), which indicates that most parameter pairs are at most weakly related to each other, suggesting that most of the parameters are approximately uncorrelated. One exception is a positive association ($r = 0.71$) between start elevation and elevation angle θ of the modelled trajectory. Additionally, some moderate correlations are observed between elevation and velocity ($r = -0.31$) as well as elevation and the vertical lift parameter ($r = -0.33$). These correlations indicate that parameters with respect to elevation are partly coupled and hence cannot be resolved completely independently; however, their correlation is low except for θ (Fig. 6a). The ablation parameter σ has near-zero correlations with the other parameters (maximum $|r| \sim 0.17$), which indicates that it contributes mostly independent information. The lift-parameter β has only weak-to-moderate correlations except for elevation, indicating its role as a nearly independent parameter in the modelling.

The covariance structure (see Fig. 6b) is consistent with the correlation patterns. Due to the different physical units of the parameters, there are scaling effects which complicate the interpretation of absolute values. Again, the largest relative covariances involve elevation with a positive covariation with elevation angle (cov ~ 0.488) and azimuth (cov ~ 0.139) and negative covariation with velocity (cov ~ -0.236). In contrast, the ablation and lift parameters have near-zero covariances with respect to most other parameters, which indicates a largely independent resolution behaviour.

The final average arrival time residual (RMSE), using the modified ray model approach, is 6. 4 s, compared to 10. 9 s using the geometrical method, achieving a c. 40 per cent improvement of the fit. In addition, the ray model can explain 41 additional arrival times (altogether 202 data), using the same culling technique as for the geometrical model with discarding arrival time residuals exceeding 20 s, while achieving the lower RMSE. If we allow an RMSE of 10. 9 s as for the geometrical model solution, the ray model can explain even 216 out of 226 arrival time data. This difference corresponds to a 34 per cent enhancement of usable input data in the ray modelling relative to 161 usable data for the geometrical model and results in an RMSE of 10. 7 s. This comparison demonstrates the superior robustness of the ray model relative to the geometrical model due to the inclusion of wind, a stratified atmosphere and more realistic ray paths taking into account β and σ (for selected ray paths, see Fig. S3 in Supplementary Material). The spatial data distribution (see Fig. 7) and the ratio of 27 between data samples and parameters also indicates a stable and well-posed inversion problem.

Uncertainty bounds for the ray model solution are estimated based on the 500 best-fitting models with the lowest arrival time residuals. The distribution of the input parameters within this subset is analysed to derive the uncertainty bounds for each parameter. This approach assumes that models with lower misfits are more likely to reflect realistic parameter combinations. Because the input parameters are normally distributed, we use the standard deviation of the parameters to estimate the uncertainty bounds (see Table 1).

Both A-S models, geometrical and ray, capture most of the length of the satellite re-entry trajectory, while both optical trajectory reconstructions, IMO (2024) and FRIPON (2024; F. Colas *et al.* 2020), yield only short subsets of the satellite trajectory. The IMO trajectory most likely fails to cover the whole length of the re-entry trajectory, due to a limited number of observations at the edges of the trajectory, while the FRIPON trajectory is clearly limited by the low number of active cameras (2; see FRIPON 2024) and the very shallow elevation angle of the re-entry. Using the IMO and FRIPON trajectories, we evaluate their fit to our acoustic-seismic data set. These calculations result in RMSE values of 2803 and 2415 s forall 226 arrival times, respectively. Compared to our ray and geometrical models with RMSE around 10 s, we propose that the latter ones should be preferred, because they should better recover the whole length of the re-entry trajectory.

4.2 Finite difference modelling of wave propagation

We use 3-D acoustic and seismic wavefield modelling to analyse the effects of deceleration and the resulting bending of the trajectory due to gravity with our best-fit ray model trajectory (Figs 7c and d). Because the angle with which the acoustic Mach waves are radiated from the satellite is inversely related to the satellite velocity, a decrease in satellite velocity leads to an opening of the Mach Cone (A. Sasoh 2020). We can observe this change in opening angle in the ray-, as well as the wave-based approach (see Figs 6b and c, Fig. 8). Modelling details are given in Text S5 (Supplementary Material).

As expected, the finite difference modelling (FDM) results reveal that as the satellite slows down, the Mach Cone opening angle increases, consistent with the theoretical expectation that the angle depends inversely on the Mach number. The synthetic wavefield snapshots (Figs 8a–d) illustrate the broadening of the cone and the resulting wider ground footprint of the direct acoustic wave. At 173. 8 s (Fig. 8a) there is still a near cylindrical Mach Cone wave front with a narrow opening angle. After about 213. 8 s the satellite reaches the end of the trajectory, see red dots in Figs 8(a)–(d), where most of the material is ablated and the velocity reaches subsonic speeds. The modelled wavefield confirms that the trajectory bends downwards more sharply during the final re-entry phase due to increased drag and deceleration, as the shock front weakens and the supersonic Mach carpet (see Fig. S4 in Supplementary Material) decreases in size. The combination of the downward bend and the opening leads to an asymmetric Mach Cone shape. After 312.8 s this bending results in a shift of the first ground coupling area away from the end of the trajectory towards the bend direction (Fig. 8c). Simplified trajectory estimations (e.g. J. Pujol *et al.* 2005) ignore this effect which gets quite significant depending on the incidence angle and velocity of the object. Fig. 8(d) shows the produced seismic signals which travel much faster than the acoustic waves. This modelling supports the trajectory reconstruction and explains arrival time discrepancies that arise, if Mach Cone opening is neglected as well as the complexity of the wavefield.

Fig. 9 summarizes how the FDM compares with the ray model for the best-fit trajectory. In Fig. 9(a), the coloured triangles represent the ray-traced arrival times while the coloured circles/area show the FDM arrivals sampled on a regular grid. Both methods reproduce the characteristic Mach carpet pattern of arrival times, confirming that the overall source–receiver geometry is correctly captured. A slight, nearly uniform negative time shift of the FDM arrivals with respect to the ray model solution is evident, which we attribute primarily to the resolution limit of the FDM.

Fig. 9(b) maps the residuals (t_{wave}–t_{ray}) between the wave and the ray models. Despite the fundamentally different nature of the two approaches, the resulting residuals remain small (typically within ∼1–2 s, with larger residuals in the area of the over-the-top Mach Cone arrivals) but become increasingly negative towards the eastern, terminal part of the path. This difference may be due to numerical resolution. In the ray model, which is a linear, high-frequency approximation, the Mach-cone opening angle is determined by the Mach number along the trajectory. In contrast, the finite-difference simulation, which is also linear in acoustics, forms the Mach cone wavefront as a superposition/interference pattern from distributed source points along the path, while propagating the full 3-D wavefield explicitly on the numerical grid. With a near-surface sound speed of 344 m s^{-1}, a 1 s traveltime residual corresponds to about 344 m of path length, that is, approximately 1.38 times the receiver grid spacing (250 m). This places the typical misfit close to the effective resolution limit of the wave simulation. Overall, the small residuals indicate that the ray model can accurately capture

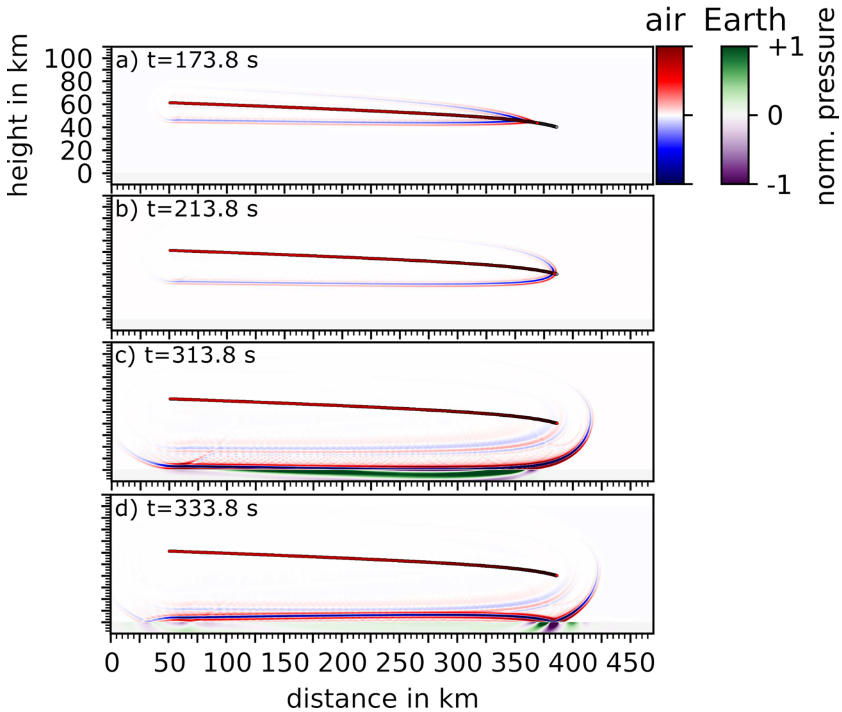

Figure 8. Time evolution of the wavefield generated by the Starlink Satellite while travelling through the atmosphere, here in a vertical plane along the trajectory (distance versus height). Normalized pressure is visualized at four time snapshots. The time t is relative to 19:28 UTC: (a) $t = 173.8$ s: the object travels at high altitude with a narrow Mach Cone, indicating supersonic speed. (b) $t = 213.8$ s: the trajectory curves downward and deceleration begins, resulting in a broader Mach Cone. (c) $t = 313.8$ s: the broadened Mach Cone leads to the first acoustic coupling with the Earth's surface, occurring away from the trajectory end point. The acoustic wave arrives after 312. 8 s at the surface. (d) $t = 333.8$ s: seismic waves travel through the Earth. Red dots mark the already triggered source points along the trajectory (flightpath and position). White dots mark the following source points (future trajectory).

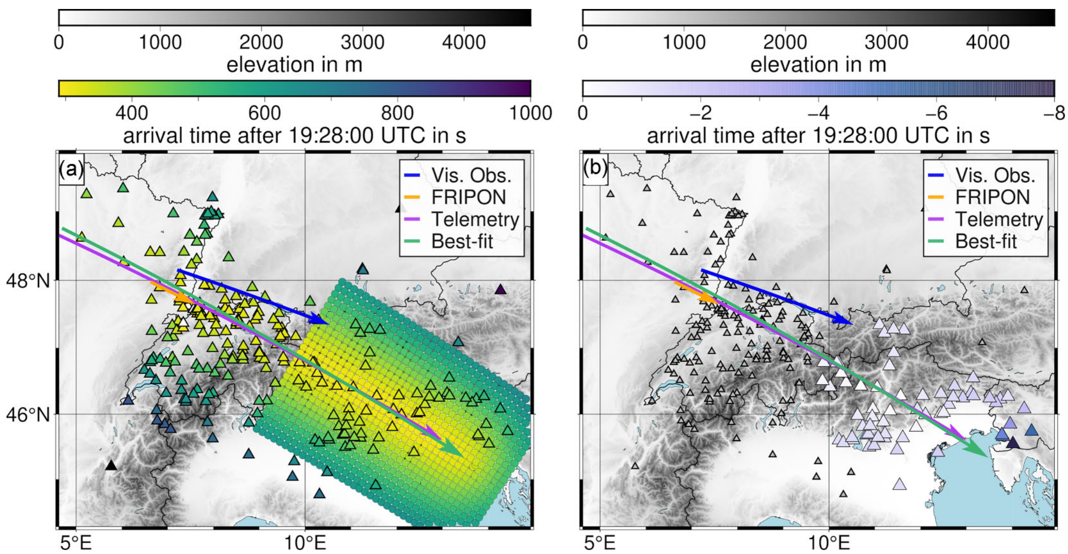

Figure 9. (a) Comparison between the ray model arrival times (coloured triangles) and the FDM arrival times (coloured area). For this model comparison a vertically layered atmosphere model without wind is used. The arrival pattern from the Mach cone is well reproduced by the modelling, although slightly shifted, compared to previous figures because of the deliberate omission of wind effects. (b) Arrival time difference between ray and FDM (bluish shading). There is a small systematic offset, due to the fundamental difference between high-frequency ray approximation and low-frequency FDM. The arrival time differences towards the end of the trajectory show that the ray modelling might not be able to account for the full complexity of the wavefield due to the Mach Cone opening (Fig. 8). Trajectories as in Fig. 7(d).

Table 2. Parameters to estimate ground compliance.

Surface material	Station pairs	E in GPa	ν	K_ν in m s^{-1} Pa^{-1} at $c = 343$ m s^{-1}	c_{AS} in m s^{-1} Pa^{-1}
Unconsolidated soft rock	AM.R2F1D & CH.DAGMA	4	0.25	1.6×10^{-7}	0.98×10^{-7}–5.86×10^{-7}
	AM.R03EA & CH.ZUR				
Consolidated hard rock	AM.R489A & CH.SARD	55	0.2	1.2×10^{-8}	4.31×10^{-10}–3.96×10^{-8}
	AM.R54F9 & OX.BOO				
	AM.R06CE & CH.SGRA				
	AM.RCDB6 & CH.SUSI				
	AM.RA038 & OE.WTTA				

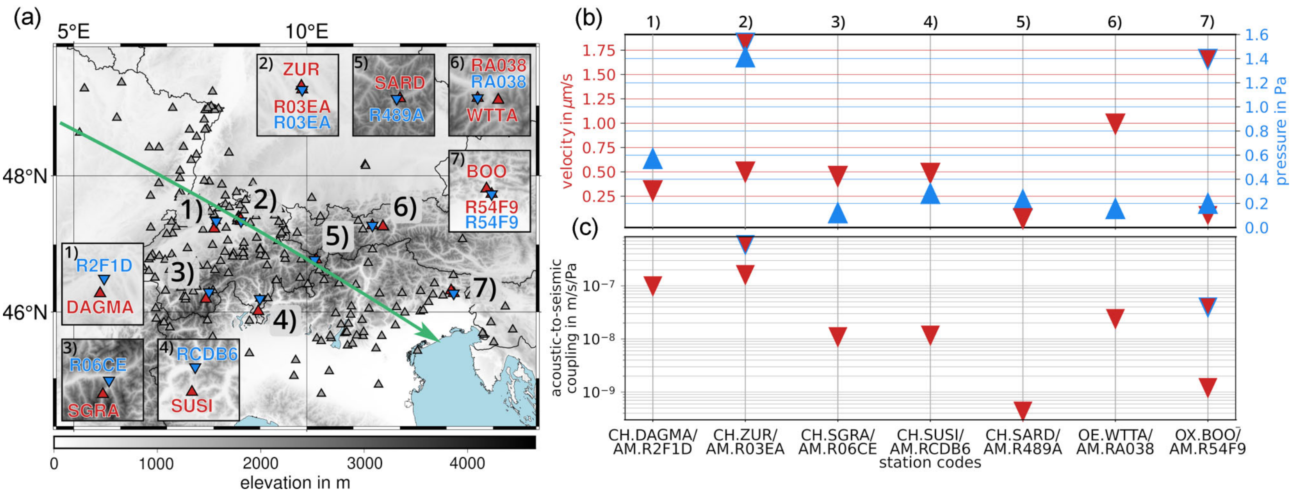

Figure 10. (a) Map of collocated A-S recording sites numbered from 1 to 7 with detail-view in related inset plots. Seismic stations are indicated with red triangles and infrasonic stations with inverted blue triangles. (b) Diagram of measured seismic ground velocity (red triangles) and acoustic overpressure (blue inverted triangles). Raspberry Shake & Boom stations with both, seismic velocity and acoustic overpressure measurements, are marked with blue-framed red triangles. The station pairs are ordered according to the respective origin time of the associated acoustic wave. (c) Diagram of acoustic-to-seismic coupling coefficients for each recording pair. The colour-coding is the same as in panel (b).

the far-field travel times of the sonic boom in the linear acoustic regime. However, close point-by-point comparisons are sensitive to modelling choices, such as source discretization, receiver spacing and the imposed versus emergent representation of the Mach cone wavefront, particularly in regions dominated by complex wave arrivals.

4.3 A-S ground coupling

To estimate the minimum ground compliance K_ν, we follow the approach by B. Fernando *et al.* (2024a) and B. Kenda *et al.* (2020) for six collocated A-S station pairs (see Table 2, Fig. 10). K_ν is given by

$$K_\nu = 2c\frac{1-\nu^2}{E}, \tag{7}$$

where E is the Young's modulus, ν is the Poisson ratio and c is the advection speed of the pressure loading. To choose the elastic properties for the station pairs we separate them into two groups: Case (1) unconsolidated soft rock, which is found in the Molasse region north of the Alps and case (2) consolidated hard rock, which is found inside the mountain range of the Alps.

Following B. Fernando *et al.* (2024a), we use a speed of the local sound at the Earth's surface of 343 m s^{-1}. Using eq. (7), the values of Table 2, and the measured peak ground velocity amplitudes (Fig. 10) of the vertical components of the respective seismograms we can derive the minimum A-S ground coupling coefficient (c_{AS}) for each station site. We find that the c_{AS} values range between 0.98×10^{-7} and 5.86×10^{-7} m s^{-1} Pa^{-1} for soft rock sites and between 4.31×10^{-10} and 3.96×10^{-8} m s^{-1} Pa^{-1} for hard rock sites. Thus, at unconsolidated, soft rock sites, there seems to be a 1–3 order of magnitude increased amplitude excitation. This agrees well with the results of B. Fernando *et al.* (2024a) and W.N. Edwards *et al.* (2007) who calculated minimum c_{AS} values of 1.4×10^{-6} and $7.3 \pm 0.2 \times 10^{-6}$ m s^{-1} Pa^{-1}, respectively, for even softer material at the Earth's surface. A. Novoselov *et al.* (2020) found c_{AS} values of 1.99–2.74 $\times 10^{-6}$ m s^{-1} Pa^{-1} for water-saturated limestone-rich material.

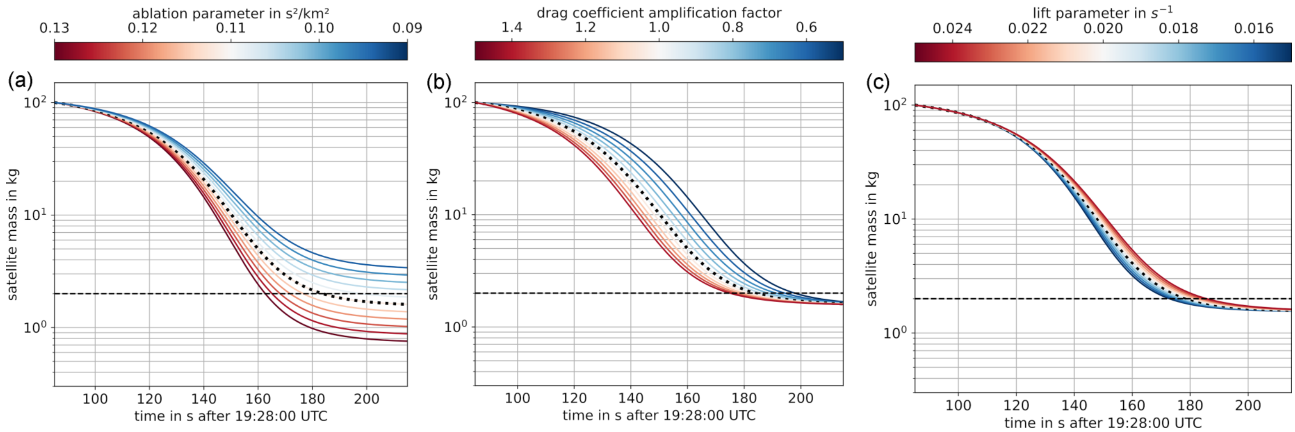

Figure 11. (a) Influence of the ablation parameter σ on the mass of the satellite fragment versus time. The different colours represent the ablation parameter within the error bounds (shown in Table 1). The dotted line represents the mass over time behaviour of the best-fit run with $m = 100$ kg, $\sigma = 0.11$ s^2 km^{-2} and a lift parameter $\beta = 0.02$ s^{-1}. The horizontal dashed black line represents the cut-off mass of 2 kg. Lighter line colours represent closer values to the best-fit ray model trajectory. This representation is the same in panels (b) and (c). Panel (b) shows the influence of the drag coefficient on the satellite fragment mass-time distribution. Different coloured lines show different drag coefficient amplification values. Panel (c) shows the influence of the lift parameter β on the satellite fragment mass-time distribution. Different coloured lines show different lift parameter values.

Knowledge about the acoustic-to-seismic coupling efficiency at seismic stations can help to constrain the masses of future events (D.O. ReVelle 1976; W.N. Edwards *et al.* 2008), where *a priori* information of the object mass such as for meteoroid events is unknown and infrasound is not available.

4.4 Ablation estimation

The unique Starlink-2382 data set can be used to study the mass loss (see eq. 5) of the satellite during the re-entry to investigate the premise that it should fully burn up. SpaceX targets a kinetic impact energy of <3 J (P. SpaceX 2025). As we use acoustic wave generation, we chose a slightly different metric in determining a full burn up of the 100 kg main fragment. We consider the satellite to be fully burned up, as soon as it falls below 2 kg in mass as per our modelling. For infrasonic data it can be assumed that objects with masses > 1 kg are reliably visible on acoustic recordings (D.O. ReVelle 1976), to account for the seismic stations we adjust our lower limit mass threshold to 2 kg. However, a 2 kg fragment at terminal velocity of c. 90 m s^{-1} would have a kinetic energy of 8100 J >> 3 J. This means that even if the satellite loses 99 per cent of its original mass, it is still possible that some material survives to the end of the modelled satellite fragment trajectory, at around 40 km altitude.

For the modelled best-fit trajectory the main satellite fragment reaches this threshold after 180 s after the reference time of 19:28:00 UTC. After c. 200 s the mass of the satellite diminishes to a mass of ∼1. 5 kg (see Fig. 11a). Considering the uncertainty for estimating the ablation coefficient σ, we find that the lower end of our retrieved range, that is, $\sigma < 0.09$ s^2 km^{-2} produces a terminal mass > 2 kg. Therefore, it is yet inconclusive if the satellite fully burned up from our modelling alone. Nevertheless, we consider the occurrence of satellite fragments with masses > 2 kg to be unlikely, because:

(i) The use of a purely spherical body is too simplistic, a more irregular rectangular shape would increase the drag coefficient, resulting in a greater mass loss for the same ablation coefficients.

(ii) As the re-entry was uncontrolled, it might make sense to try to model an erratic tumbling motion of the main satellite fragment which also increases its drag coefficient and mass loss. This is indirectly covered with the introduction of the lift parameter β, that is based on the spinning motion of the satellite fragment. While higher β values decrease the mass loss over time, its value has negligible effect on the final mass of the satellite fragment (see Fig. 11c).

(iii) Video material of the re-entry shows an increase of individual fragments with time during the re-entry (Table S2 in Supplementary Material), which means that neglecting fragmentation of the satellite fragment might be too simplistic. Even though the mass loss attributed to the break-off of the solar panels is factored in already and we deliberately model only the c. 100 kg main mass, we cannot be certain that not more material is subject to breaking off from the main mass during re-entry. This would decrease the mass of the main body that is most likely generating the acoustic waves that we analysed in this study. A mass decrease would in turn then result in a more likely burn-up with the same ablation coefficient.

Due to (i) the best-fit, ablation parameter should be viewed as an effective ablation parameter for the Starlink satellite. The true ablation parameter can only be derived from modelling, like the one presented in this study, if the shape and composition of the satellite is known and accounted for more thoroughly. Fig. 11 shows the influence of the ablation parameter σ, the drag coefficient Γ and the lift parameter β on the satellite fragment mass over time based on the best-fit ray model trajectory. To simulate different drag coefficients,

Table 3. Comparison of ablation coefficients σ between re-entry events and meteoroids.

Event	Initial mass in kg	Initial velocity in km s^{-1}	Ablation coefficient in s^2 km^{-2}
Starlink-2382 main fragment (this study)	c. 100	c. 10.5	0.11 ±0.02
39048 [a]	c. 12	22.143	0.19
Chelyabinsk meteoroid	1.3e7 ± 1e2 [b]	19.16 ± 0.3 [b]	0.034 [c]
Neuschwanstein meteoroid [d]	600	21	0.018 ± 0.002
Morávka meteoroid [e]	1500	22.5	0.003
Hayabusa sample return capsule [f]	20	12	0.0014 ± 0.001

[a]Z. Ceplecha *et al.* 1998.
[b]O. Popova *et al.* 2013.
[c]J.M. Trigo-Rodríguez *et al.* 2021.
[d]P. Spurny *et al.* 2003.
[e]J. Boroviĉka & P. Kalenda 2003.
[f]J. Boroviĉka *et al.* 2011.

we vary these by ±50 per cent and find that this results in ca. ± 15 s time for burn-up. To estimate the effect of the lift parameter on the mass loss of the satellite fragment, we simulate lift parameter values within the uncertainty bounds between 0.015 and 0.025 s^{-1}. We find that an increased lift parameter results in a decreased mass loss rate along the trajectory. This is due to the increased traveltime through the less dense higher atmosphere, when the satellite fragment experiences the additional lift. The estimated best-fit effective ablation coefficient value of 0.11 s^2 km^{-2} is within the upper range of values typically found for natural meteoroids with typical ablation coefficients between 0.014 and 0.19 s^2 km^{-2} (Z. Ceplecha *et al.* 1998). Table 3 provides a comparative analysis. Starlink-2382 displays effective ablation coefficient values that are an order of magnitude higher, peaking at approximately 0.11 s^2 km^{-2} compared to the Chelyabinsk and Neuschwanstein meteoroids at c. 0.034 and 0.018 s^2 km^{-2}, respectively. It aligns better with meteoroids with higher ablation coefficient values and low bulk densities like, for example, meteoroid 39 048 (see Table 3). This is consistent with the design intent of Starlink satellites to fully disintegrate upon re-entry (SpaceX 2025), suggesting a higher surface area-to-mass ratio and greater susceptibility to drag-induced ablation. Additionally, the simplifying assumptions in our model, for example, spherical symmetry, likely underpredict the true mass loss. This can be further illustrated by the comparison of the Starlink satellite to the Hayabusa sample return capsule, which was engineered for controlled re-entry and landing, with its low-ablation coefficient of only 0.0014 s^2 km^{-2} (J. Boroviĉka *et al.* 2011).

5. DISCUSSION

The reconstruction of the Starlink-2382 re-entry event trajectory is significantly improved by the ray model incorporating atmospheric stratification, wind effects, the ablation of the satellite and a vertical lift parameter β. In comparison with the geometrical model (J. Pujol *et al.* 2005; D. Vida 2023), the application of the ray model achieves a reduction in RMSE residuals of approximately 40 per cent (from 10. 9 to 6. 4 s), whilst simultaneously expanding the number of usable arrival times by over 30 per cent (see Table 1). This enhancement is of particular significance when considering the complex acoustic propagation environment encountered during re-entry, where assumptions of a uniform atmosphere or linear ray paths frequently result in systematic misfits, especially for flat-angle incident objects.

The incorporation of the β parameter, a vertical perturbation term, yields a trajectory more consistent with the wave arrivals observed at the surface. The parameter helps to mitigate residual trends along the trajectory. Although its physical origin remains partly uncertain, β may reflect aerodynamic lift or torque-related forces such as the Magnus effect arising from satellite spin (J. Elliott *et al.* 2024; S. Mancuso *et al.* 2024). Because rotational state and torque of Starlink-2382 are unknown to us and thus not explicitly modelled here, β should be interpreted as an effective parameter. Future investigations could focus on isolating this effect through controlled experiments or additional modelling of the rotational effects.

The trajectory uncertainty analysis, based on 500 models, provides a stable best-fit and its narrow range further supports the robustness of the ray model result within the assumptions and trajectory parametrization. As demonstrated in Table 1, the initial parameters, including longitude, latitude and velocity, exhibit a high degree of convergence with low uncertainty. This finding suggests that infrasound and seismic data, when integrated with realistic trajectory physics, has the capacity to provide precise constraints on initial re-entry conditions.

Our finite-difference wavefield simulations confirm the ray-based modelling and demonstrate that the downward bend in the final trajectory phase, combined with the Mach Cone opening, results in a complex acoustic wave arrival pattern (Figs 8 and 9). This provides a plausible explanation for the spatial mismatch between expected and observed arrivals when static Mach angles are assumed. It also provides a physical explanation for several anomalous arrival times, especially at the end of the trajectory. However, these interpretations should be regarded as indicative rather than definitive because the current finite-difference simulations cannot include all relevant physical processes, such as wind affecting acoustic wave propagation and full 3-D thermodynamic variability. Incorporating these processes into future models is important for quantifying their relative contributions and avoiding systematic biases in source location estimates for artificial and natural atmospheric entry events, particularly at low-entry angles.

Our analysis of acoustic-to-seismic coupling across seismic stations reveals strong site-dependent variability in the acoustic-to-seismic ground coupling coefficient c_{AS}. Using elastic parameters and peak ground motion amplitudes (Table 2), we estimate c_{AS} values ranging from 0.98×10^{-7}–5.86×10^{-7} m s^{-1} Pa^{-1} on soft, unconsolidated rock material, compared with significantly lower values (4.31×10^{-10}–3.96×10^{-8} m s^{-1} Pa^{-1}) on hard rock. These findings are consistent with previous studies (W.N. Edwards *et al.* 2007; A. Novoselov *et al.* 2020; B. Fernando *et al.* 2024a) and emphasize the role of surface geology in modulating signal amplitude. This variability must be accounted for when using seismic amplitudes to infer source parameters such as energy or mass (D.O. ReVelle 1976). Ignoring local geological effects at a seismometer site may introduce large systematic errors, particularly for events lacking infrasound or optical data. While not explicitly observable in our data, the c_{AS} values are possibly frequency- and azimuth-dependent. To better understand these coupling effects, additional studies are needed, however.

Our modelling indicates an effective ablation coefficient for Starlink-2382 that is one to two orders of magnitude higher than for typical meteoroids. This relatively high value is consistent with the satellite's deliberate design to disintegrate efficiently during re-entry. However, our modelling indicates that some material could have survived into the late stages of the modelled trajectory, and our rough kinetic energy estimate may be orders of magnitude above the upper limit reported by SpaceX (SpaceX 2025). However, this comparison is highly sensitive to our modelling assumptions and should be treated with caution. Although our modelling cannot confirm complete disintegration, the high effective ablation coefficient supports the likelihood of a 99 per cent mass loss of the satellite during re-entry (Fig. 11). Furthermore, our use of a simplified spherical geometry likely underestimates atmospheric drag and mass loss by ablation. Better estimates of satellite-specific geometry, tumbling behaviour and fragmentation, would likely increase the effective ablation rate.

These results emphasize the necessity of incorporating object-specific physical characteristics in ablation models. As an artificial satellite can reach the upper values of the expected ablation efficiency of natural meteoroids, this implies that meteoroid modelling assumptions cannot be universally applied to artificial re-entry events. This distinction is crucial for future atmospheric entry reconstructions involving space debris.

6. CONCLUSIONS

This study presents a refined reconstruction of the atmospheric trajectory and acoustic wave generation related to the re-entry of the Starlink-2382 satellite in August 2024. The high-seismic station density in Central Europe and the low-elevation angle with a downward wave emission both lead to a very high number of 226 usable observations, which allows a well-constrained trajectory reconstruction approach. Our preferred reconstruction is based on a novel ray-based iterative damped direct search approach using the infraGA software (Y. Blom 2014). Incorporating a 3-D atmospheric wind model, ablation to model the time-dependent mass, and a lift-like force enables us to achieve a significantly better fit to acoustic and acoustic-to-seismic coupled arrival times compared to geometrical trajectory modelling. The ray model reduces average arrival time residuals by ~40 per cent compared to the more commonly used geometrical model approach (J. Pujol *et al.* 2005; D. Vida 2023) with linear ray geometries. The more realistic 3-D ray path modelling also fits more data (34 per cent in our case with a cut-off at 20 s residual), enabling a more robust and comprehensive trajectory estimation. In this specific case, the acoustic-seismic trajectory reconstruction yields a better fit to the measured data than optical trajectory estimates.

Finite-difference simulations of the emitted acoustic wavefield provide an independent benchmark for the dynamic ray-based reconstruction of the trajectory. Consistency between both approaches indicates that the ray model can accurately capture the far-field traveltimes of the sonic boom in the linear, acoustic regime. In this context, the shadow zones, which can arise in infraGA due to ray approximations and low-velocity layers, do not appear to significantly impact the results. The wavefield simulations also reveal the Mach Cone opening and the influence of the trajectory bending. These effects can significantly affect acoustic arrival patterns, and their traveltime anomalies must be incorporated into future models to avoid a mislocation of extraterrestrial sources or a misinterpretation of the related phase arrival times. However, an acoustic wavefield modelling including wind is currently not feasible, due to the lack of modelling capabilities at present. The bending during the terminal flight, often without light emissions and thus called dark-flight phase, is especially important for objects with a low entry angle and could be observed with acoustic and seismic measurements. Such objects, that is, shallow-entry meteoroids do not completely burn up and can thus be picked up at the Earth's surface. Nevertheless, correct modelling using the acoustic rays can narrow down the strewn field, optimizing search areas to recover precious meteorite material. This is particularly relevant for cosmic studies, such as astrobiology, where the swift recovery of meteorites is crucial for studying extraterrestrial amino acids (e.g. D.P. Glavin et al. 1999) or rare isotopes before terrestrial weathering begins.

Our determined effective ablation coefficient of 0.11 ± 0.02 s^2 km^{-2} corresponds to the upper end of values expected for typical meteoroids. Such a high value is consistent with an intentional design that allows for substantial burn-up upon re-entry. Since we chose to model a spherical body, so that we could apply Mach number dependent drag coefficients, the ablation coefficient remains an effective ablation coefficient for the modelled satellite fragment. To find the true ablation coefficient of the satellite more detailed studies must be made. More such studies should be done in order to better calibrate the determination of ablation for meteoroids with acoustic-seismic data for which the mass, geometry and material properties are not known.

The found variation in the coupling coefficient of 4.31×10^{-10}–5.86×10^{-7} m s^{-1} Pa^{-1} depends on the local surface geology of the recording site. Of course, there remain uncertainties, particularly in how coupling efficiency depends on wavefront incidence angles and azimuth. To improve the use of amplitude information from measured extraterrestrial material, for example, to estimate their energy or mass, more controlled-source experiments could be carried out to study the azimuth dependency of the ground coupling coefficients. More acoustic sensors at seismic sites should be used for the determination of empirical coupling coefficients at selected sites.

A significant advantage of our studied event is that the initial mass of the Starlink-2382 satellite is precisely known (approximately 260 kg in a fully fuelled state) in contrast to natural meteoroid entries. This unique opportunity allows us to calibrate models of acoustic energy generation and mass loss against a controlled reference, however the fragmentation (see Fig. S1 and Table S2 in Supplementary Material) poses an uncertainty in the mass parameter. The increasing number of satellites in low Earth orbit is likely to result in a higher frequency of uncontrolled re-entry events of similar nature.

Overall, a future challenge is the calibration of seismic stations for consistent retrieval of source energy or mass of extraterrestrial objects with acoustic waves. Signal amplitudes are affected by surface geology, atmospheric path effects, wavefront geometry and coupling dynamics. This study establishes a benchmark for future calibration efforts of this kind and demonstrates the value of combining multidisciplinary observational data with advanced modelling techniques.

SUPPORTING INFORMATION

Supplementary data are available at *GJIRAS* online.

Please note: Oxford University Press are not responsible for the content or functionality of any supporting materials supplied by the authors. Any queries (other than missing material) should be directed to the corresponding author for the article.

ACKNOWLEDGMENTS

We thank reviewer Benjamin Fernando and an anonymous reviewer for helpful advice which improved the original manuscript. We acknowledge funding by the Vector Stiftung, Stuttgart, through project '*Seismologische Detektion von Meteoren—SeisMET*'. J-PF was partly supported by grant no. FKZ: 03F0952C of the German Federal Ministry of Research, Technology and Space (BMFTR) as part of the DAM mission 'mareXtreme', under the project MULTI-MAREX. We are thankful for the ability to use of the high-performance computing infrastructure at the Geophysical Institute of KIT, as well as the technical support by Thomas Hertweck and Michael Frietsch. Open Access publications costs are paid by KIT Bibliothek.

AUTHOR CONTRIBUTIONS

D.E. (Conceptualization, Methodology, Software coding, Writing—original-draft), J.-P. F. (Finite-difference methodology, Waveform modelling and coding, Writing—original-draft) and J.R. (Conceptualization, Funding—acquisition, supervision, writing—original-draft).

DATA AVAILABILITY

All used waveform data available. Waveform data can be retrieved via ObsPy, see network references below. Waveform data of the KB network must be accessed via the FDSN web service https://ws.gpi.kit.edu/. Wind data can be retrieved with the NCPAG2S Command-Line Client. Maps were created with PyGMT.

SOFTWARE REFERENCES

InfraGA/GeoAc: Blom, P., 2014. "Infraga/geoac," https://github.com/LANL-Seismoacoustics/infraGA ((accessed March 2025).

NCPAG2S-CLC: Hetzer, C.H., 2024. "The NCPAG2S Command-Line Client,". https://github.com/chetzer-ncpa/ncpag2s-clc. https://zenodo.org/records/13345069. (accessed May 2026).

ObsPy: Beyreuther, M., Barsch, R., Krischer, L., Megies, T., Behr, Y. & Wassermann, J., 2010. ObsPy: a Python toolbox for seismology, *Seismol. Res. Lett.,* **81**(3), 530–533.

PyGMT: Uieda, L. *et al.*, 2021. PyGMT: a Python interface for the generic mapping tools, https://doi.org/10.5281/ZENODO.4522136. (accessed May 2026).

PySwarms: Miranda, L.J., 2018. PySwarms: a research toolkit for Particle Swarm Optimization in Python, *J. Open Source Software,* **3**(21), 433. https://doi.org/10.21105/joss.00433

WAVE: Qin, T. & Bohlen, T., 2022. WAVE-Toolbox, https://github.com/Tan-Qin-2019KIT/WAVE-Simulation (accessed October 2023).

NETWORK REFERENCES (FDSN)

4P: AdriaArray Temporary Network: Italy—north, south, The Italian National Institute of Geophysics and Volcanology (INGV).

8D: Swiss Seismological Service (SED) At ETH Zurich, 2005. *Temporary deployments in Switzerland associated with aftershocks and other seismic sequences,* ETH Zurich.

Swiss Seismological Service (SED) At ETH Zurich, 2012. 9S: temporary deployments in Switzerland associated with landslides, ETH Zurich.

AM: Raspberry Shake, S.A., 2016. *Raspberry Shake,* International Federation of Digital Seismograph Networks.

BW: Department of Earth and Environmental Sciences, Geophysical Observatory, University of Munchen, 2001. *BayernNetz,* International Federation of Digital Seismograph Networks.

CH: Swiss Seismological Service (SED) At ETH Zurich, 1983. *National Seismic Networks of Switzerland,* ETH Zürich.

FR: Epos-France Seismology, 1995. *Epos-France Broad-band network (RLBP),* Epos-France Seismological Data Centre.

G2: Swiss Seismological Service (SED) at ETH Zurich, 2006. *GEOBEST Baseline Seismic Monitoring Networks for Deep Geothermal Energy Projects in Switzerland,* ETH Zurich.

GQ: german Strong Earthquake Nework.

GR: Federal Institute for Geosciences and Natural Resources, 1976. *German Regional Seismic Network (GRSN),* Bundesanstalt für Geowissenschaften und Rohstoffe.

GU: University of Genoa, 1967. *Regional Seismic Network of North Western Italy [Data set],* International Federation of Digital Seismograph Networks.

IV: Istituto Nazionale di Geofisica e Vulcanologia (INGV), 2005. *Rete Sismica Nazionale (RSN),* Istituto Nazionale di Geofisica e Vulcanologia (INGV).

KB: karlsruhe BroadBand Array (KABBA), Available via https://ws.gpi.kit.edu/

MN: medNet Project Partner Institutions, 1990. *Mediterranean Very Broadband Seismographic Network (MedNet),* Istituto Nazionale di Geofisica e Vulcanologia (INGV).

NI: OGS (Istituto Nazionale di Oceanografia e di Geofisica Sperimentale) and University of Trieste, 2002. *North-East Italy Broadband Network,* International Federation of Digital Seismograph Networks.

OE: ZAMG—Zentralanstalt für Meterologie und Geodynamik, 1987. *Austrian Seismic Network,* International Federation of Digital Seismograph Networks.

OX: Istituto Nazionale di Oceanografia e di Geofisica Sperimentale—OGS, 2016. *North-East Italy Seismic Network,* FDSN.

RD: RESIF, 2018. *CEA/DASE broad-band permanent network in metropolitan France,* RESIF—Réseau Sismologique et géodésique Français.

SI: province Südtirol.

SL: Slovenian Environment Agency, 1990. *Seismic Network of the Republic of Slovenia,* International Federation of Digital Seismograph Networks.

ST: Geological Survey-Provincia Autonoma di Trento, 1981. *Trentino Seismic Network,* International Federation of Digital Seismograph Networks.

ZO: Massa, M., Rizzo, A. L., Lorenzetti, A., Lovati, S., D'Alema, E., Puglia, R., Carannante, S. & Luzi, L., 2021. *Rete di monitoraggio multiparametrico del Garda (Nord Italia)—PDnet (Version 1.0),* Istituto Nazionale di Geofisica e Vulcanologia (INGV).

REFERENCES

Ailor, W.H., 2019. Hazards of reentry disposal of satellites from large constellations, *J. Space Safety Eng.,* **6**(2), 113–121.

Arrowsmith, S.J., Drob, D.P., Hedlin, M.A. & Edwards, W., 2007. A joint seismic and acoustic study of the Washington State bolide: observations and modelling, *J. Geophys. Res.: Atmos.,* **112**(D9).

Blom, P., Gammans, C., Delbridge, B. & Carmichael, J.D., 2024. Prediction of regional infrasound produced by supersonic sources using a ray-based Mach cone source, *J. Acoust. Soc. Am.,* **155**(3), 1667–1681.

Boley, A.C. & Byers, M., 2021. Satellite mega-constellations create risks in Low Earth Orbit, the atmosphere and on Earth, *Sci. Rep.,* **11**(1), 10 642.

Boroviĉka, J., Abe, S., Shrbený, L., Spurný, P. & Bland, P.A., 2011. Photographic and radiometric observations of the HAYABUSA re-entry, *Publ. Astron. Soc. Japan,* **63**(5), 1003–1009.

Boroviĉka, J. & Kalenda, P., 2003. The Morávka meteorite fall: 4. Meteoroid dynamics and fragmentation in the atmosphere, *Meteorit. Planet. Sci.,* **38**(7), 1023–1043.

Campbell-Brown, M.D., Borovička, J., Brown, P.G. & Stokan, E., 2013. High-resolution modelling of meteoroid ablation, *Astron. & Astrophys.,* **557,** A41.

Carter, R.T., Jandir, P.S. & Kress, M.E., 2011. Constraining the drag coefficients of meteors in dark flight, *Meteoroids: The Smallest Solar System Bodies, Proceedings of the Meteoroids Conference*. NASA.

Cates, J.E. & Sturtevant, B., 2002. Seismic detection of sonic booms, *J. Acoust. Soc. Am.,* **111**(1), 614–628.

Ceplecha, Z., Borovička, J., Elford, W.G., ReVelle, D.O., Hawkes, R.L., Porubčan, V. & Šimek, M., 1998. Meteor phenomena and bodies, *Space Sci. Rev.,* **84,** 327–471.

Colas, F. *et al.*, 2020. FRIPON: a worldwide network to track incoming meteoroids, *Astron. & Astrophys.,* **644,** A53.

de Groot-Hedlin, C.D. & Hedlin, M.A., 2014. Infrasound detection of the Chelyabinsk meteor at the USArray, *Earth planet. Sci. Lett.,* **402,** 337–345.

de Groot-Hedlin, C.D., Hedlin, M.A., Walker, K.T., Drob, D.P. & Zumberge, M.A., 2008. Evaluation of infrasound signals from the shuttle Atlantis using a large seismic network, *J. Acoust. Soc. Am.,* **124**(3), 1442–1451.

Drob, D.P., Garcés, M., Hedlin, M. & Brachet, N., 2010. The temporal morphology of infrasound propagation, *Pure appl. Geophys.,* **167,** 437–453

Drob, D.P., Picone, J.M. & Garcés, M., 2003, Global morphology of infrasound propagation, *J. geophys. Res.,* **108,** 4680.

Edwards, W.N., 2009. Meteor generated infrasound: theory and observation, *Infrasound Monitoring for Atmospheric Studies,* pp. 361–414, Springer-Verlag.

Edwards, W.N., Brown, P.G. & Eaton, D.W., 2009. Frequency-dependent acoustic–seismic coupling of meteor shock waves, *Bull. seism. Soc. Am.,* **99**(5), 3055–3066.

Edwards, W.N., Eaton, D.W. & Brown, P.G., 2008. Seismic observations of meteors: coupling theory and observations, *Rev. Geophys.,* **46**(4).

Edwards, W.N., Eaton, D.W., McCausland, P.J., ReVelle, D.O. & Brown, P.G., 2007. Calibrating infrasonic to seismic coupling using the Stardust sample return capsule shockwave: implications for seismic observations of meteors, *J. Geophys. Res.: Solid Earth,* **112**(B10).

Eickhoff, D., Föst, J.-P., Ostermeier, R., Koushesh, K. & Ritter, J.R.R., 2023. Estimating a meteoroid's trajectory using seismic data: case study of the November 2017 meteoroid over Germany, *Proceedings of the International Meteor Conference 2023,* International Meteor Organization. pp. 143–145.

Eickhoff, D., Föst, J.-P. & Ritter, J., 2024. Moving sources in moving media: tracing meteoroid 2024 BX1 through Earth's atmosphere with seismoacoustic data. WGN, *Journal of the International Meteor Organization,* **52**(6), 160–163.
Elliott, J., Smith, L., Lyu, B. & Smith, B.L., 2024. The combined influence of spin and roughness frequency on sphere aerodynamics, *Exp. Fluids,* **65**(4), 60.
Fernando, B. *et al.*, 2024a. Seismoacoustic measurements of the OSIRIS-REx re-entry with an off-grid Raspberry PiShake, *Seismica,* **3**(1).
Fernando, B. *et al.*, 2024b. Array-based seismic measurements of OSIRIS-REx's re-entry, *Seismol. Res. Lett.,* **96,** 2742–2752.
Fernando, B. & Charalambous, C., 2026. Reentry and disintegration dynamics of space debris tracked using seismic data, *Science,* **391**(6783), 412–416.
Föst, J.-P., Eickhoff, D., Ostermeier, R., Koushesh, K. & Ritter, J.R.R., 2023. Towards improved seismological meteoroid localization: finite difference modelling of meteoroid induced acoustic and seismic signals, *Proceedings of the International Meteor Conference 2023,* International meteor organization. pp.146–148.
FRIPON (Fireball Recovery and InterPlanetary Observation Network), 2024. https://fireball.fripon.org/displaymultiple.php?id=23514, accessed 20.5.2025
Fuchs, K. & Müller, G., 1971. Computation of synthetic seismograms with the reflectivity method and comparison with observations, *Geophys. J. Int.,* **23**(4), 417–433.
Glavin, D.P., Bada, J.L., Brinton, K.L. & McDonald, G.D., 1999. Amino acids in the Martian meteorite Nakhla, *Proc. Natl. Acad. Sci. USA,* **96**(16), 8835–8838.
Huber, M., McWilliams, J.C. & Ghil, M., 2001. A climatology of turbulent dispersion in the troposphere, *J. Atmos. Sci.,* **58**(16), 2377–2394.
IMO (International Meteor Organization), 2024. From https://fireballs.imo.net/members/imo_view/event/2024/4700 accessed 20.5.2025
Ishihara, Y., Hiramatsu, Y., Yamamoto, M.Y., Furumoto, M. & Fujita, K., 2012. Infrasound/seismic observation of the Hayabusa reentry: observations and preliminary results, *Earth Planets Space,* **64,** 655–660.
Kanamori, H., Mori, J., Sturtevant, B., Anderson, D.L. & Heaton, T., 1992. Seismic excitation by space shuttles, *Shock Waves,* **2,** 89–96.
Kenda, B. *et al.*, 2020. Subsurface structure at the InSight Landing Site from compliance measurements by seismic and meteorological experiments, *J. Geophys. Res.: Planets,* **125**(6).
Kissling, E., Ellsworth, W.L., Eberhart-Phillips, D. & Kradolfer, U., 1994. Initial reference models in local earthquake tomography, *J. geophys. Res.,* **99,** 19 635–19 646 .
Langston, C. A., 2004. Seismic ground motions from a bolide shock wave, *J. Geophys. Res.: Solid Earth,* **109**(B12).
Lawrence, A. *et al.*, 2022. The case for space environmentalism, *Nat. Astron.,* **6**(4), 428–435.
Mahrt, L., 2011. Surface wind direction variability, *J. Appl. Meteorol. Climatol.,* **50**(1), 144–152.
Mancuso, S., Barghini, D. & Gardiol, D., 2024. Meteoroid rotation and quasi-periodic brightness variation of meteor light curves, *Astron. & Astrophys.,* **683,** L1.
McDowell, Jonathan C., 2020. The low earth orbit satellite population and impacts of the SpaceX Starlink constellation, *Astrophysical Journal Letters,* **892(2),** L36.
Nishikawa, Y. *et al.*, 2022. Modelling of 3D trajectory of Hayabusa2 re-entry based on acoustic observations, *Publ. Astron. Soc. Japan,* **74**(2), 308–317.
Novoselov, A., Fuchs, F. & Bokelmann, G., 2020. Acoustic-to-seismic ground coupling: coupling efficiency and inferring near-surface properties, *Geophys. J. Int.,* **223**(1), 144–160.
Omaly, P., Ailor, W., Pardini, C., Kenichi, S., Lips, T. & Soares, T., 2025. Hazards associated with reentry, *Acta Astronaut.,* **228,** 246–252.
Patera, R.P., 2008. Hazard analysis for uncontrolled space vehicle reentry, *J. Spacecraft Rockets,* **45**(5), 1031–1041.
Pfiffner, O.A. 2021 The Geology of Switzerland, in *Landscapes and Landforms of Switzerland. World Geomorphological Landscapes,* eds, Reynard, E., Springer-Verlag. 10.1007/978-3-030-43203-4_2
Pilger, C., Gaebler, P., Hupe, P., Ott, T. & Drolshagen, E., 2020. Global monitoring and characterization of infrasound signatures by large fireballs, *Atmosphere,* **11**(1), 83.
Popova, O. *et al.*, 2013. Chelyabinsk airburst, damage assessment, meteorite recovery, and characterization, *Science,* **342**(6162), 1069–1073.
Pujol, J., Rydelek, P. & Bohlen, T., 2005. Determination of the trajectory of a fireball using seismic network data, *Bull. seism. Soc. Am.,* **95**(4), 1495–1509.
Qamar, A., 1995. Space shuttle and meteroid–tracking supersonic objects in the atmosphere with seismographs, *Seismol. Res. Lett.,* **66**(5), 6–12.
ReVelle, D.O., 1976. On meteor-generated infrasound, *J. geophys. Res.,* **81**(7), 1217–1230.
ReVelle, D.O., 1997. Historical detection of atmospheric impacts by large bolides using acoustic-gravity waves, *Ann. N.Y. Acad. Sci.,* **822,** 284–302.
Sansom, E.K. *et al.*, 2022. The scientific observation campaign of the Hayabusa-2 capsule re-entry, *Publ. Astron. Soc. Japan,* **74**(1), 50–63.
Sasoh, A., 2020. *Compressible Fluid Dynamics and Shock Waves,* Springer-Verlag.
Satcat 2024. STARLINK-2382, 47801 (Decayed), From https://www.satcat.com/sats/47801, accessed 05.05.2025.
Silber, E.A. *et al.*, 2024. Geophysical observations of the 2023 September 24 OSIRIS-REx sample return capsule reentry, *Planet. Sci. J.,* **5**(9), 213.
SpaceX 2025. Starlink approach to satellite demisability, From https://www.starlink.com/publicfiles/Starlink_Approach_to_Satellite_Demisability.pdf accessed 03.06.2025
Spurný, P., Oberst, J. & Heinlein, D., 2003. Photographic observations of Neuschwanstein, a second meteorite from the orbit of the Příbram chondrite, *Nature,* **423**(6936), 151–153.
Trigo-Rodríguez, J.M., Dergham, J., Gritsevich, M., Lyytinen, E., Silber, E.A. & Williams, I.P., 2021. A numerical approach to study ablation of large bolides: application to Chelyabinsk, *Adv. Astron.,* **2021**(1), 8852 772.
Vida, D., 2023. Estimating fireball trajectories using seismic and acoustic data. WGN, *Journal of the International Meteor Organization,* **51**(5), 132–140.
Yamamoto, M.Y., Ishihara, Y., Hiramatsu, Y., Kitamura, K., Ueda, M., Shiba, Y., Furumoto, M. & Fujita, K., 2011. Detection of acoustic/infrasonic/seismic waves generated by hypersonic re-entry of the HAYABUSA capsule and fragmented parts of the spacecraft, *Publ. Astron. Soc. Japan,* **63**(5), 971–978.